2024 IEEE/ASME International Conference on Advanced Intelligent Mechatronics (AIM)
July 15-19, 2024. Boston, MA, USA

Analytical and Experimental Investigation of a Tunnel Magnetoresistance Sensor Array System for Permanent Magnet Tracking

Chun-Yeon Lin, *Member*, *IEEE/ASME*, Zhong-Hsiang Kuo, and Yu-Han Tsai

Abstract—**This paper presents the development of a five degree-of-freedom (DoF) cylindrical permanent magnet (PM) tracking system for estimating orientation and location. The system measures the effects of magnetic field changes caused by the PM through a tunnel magnetoresistance (TMR) sensor array. Closed-form solutions for the magnetic flux densities are derived, and the Gaussian-Legendre quadrature method is applied to enhance computational efficiency. The Levenberg–Marquardt (LM) algorithm is employed to estimate location and orientation. These closed-form solutions were verified by finite element analysis software, and the LM methods were numerically validated. Experiments with a prototype confirm the analytical model's accuracy in handling translational and angular displacements and demonstrate the validity of two cylindrical PMs' location and orientation estimations.**

I. Introduction

Magnetic tracking enables accurate positioning without the need for a line of sight. This advantage makes intrabody navigation feasible [1]. Compared to electromagnetic tracking, the permanent magnet (PM) tracking method does not require a power supply, allowing easy embedding into the tracked object [2]. Hall effect sensors were initially commonly used in magnetic sensor arrays [3]. Anisotropic magnetoresistance (AMR) has emerged as an improved solution capable of measuring three orthogonal magnetic field directions. However, the remanence effect of AMR sensors impacts measurements, necessitating an additional reset device to eliminate this effect. Exploiting the quantum tunneling effect, tunnel magnetoresistance (TMR) sensors can detect subtle changes in magnetic fields, making them suitable for applications requiring fine position sensing. TMR sensors offer a wider sensing range, low hysteresis, and temperature dependence, improving reliability under various operating conditions. Their small size and low power consumption make TMR sensors well-suited for medical, robotics, and sensing applications across various industries.

In the design of a single TMR sensor, a blinking system with an integrated magnetic sensor and an analog circuit embedded in a glass frame uses a TMR sensor to detect magnets on the eyelid, allowing repetitive blinks triggered by specific commands [4]. A displacement-based accelerometer integrating a TMR sensor with a parallel beam and an electromagnetic feedback unit has also been proposed [5]. This prototype exhibits high sensitivity and a broad sensing range, demonstrating enhanced performance in displacement-based accelerometers. The TMR sensor array ensures accurate defect classification, aiding in the advancement of non-destructive detection capabilities [6]. The efficacy of TMR sensor arrays in accurate current measurement within multi-core cables is proven by establishing a trans-impedance relationship, which aids in recovering current phases in complex multi-core systems [7]. Nonetheless, a low-cost wireless localization method using a magnetic sensor array to track PMs at the tip of a robot integrates analytics and machine learning to surpass existing techniques [8], [9]. This method addresses the challenges of shape estimation and control in expanding robots. A sophisticated PM multi degrees-of-freedom (DoF) motion-sensing system that employs a magnetic tensor sensor array and incorporates a fully connected artificial neural network (ANN) achieves accurate five-DoF motion measurements. Redundancy in measurements addresses singularity issues and enhances precision over single-sensor systems [10].

Modeling the PM magnetic field is crucial for designing a PM tracking system. The magnetic dipole approximation is a commonly used approach because it simplifies complex magnetic fields with good accuracy at large distances [11]. Lee et al. introduced distributed multipole (DMP) modeling, which retains the advantages of the magnetic dipole approximation while accounting for the shape and magnetization of the physical magnet [12]. Diverse PM movements result in varying magnetic field measurements by the sensors. Several algorithms have been proposed to address this challenge. Schlageter et al. utilized the Levenberg–Marquardt (LM) optimization algorithm with a 4×4 Hall sensor array to track the PM across five-DoF [3]. Song et al. developed a cubic sensor array using the LM optimization algorithm to estimate multiple positions and orientations of PMs [13]. The LM algorithm requires an initial guess. If the initial guess has a significant error, the algorithm may not obtain a correct global solution due to local minima [14]. Peng et al. introduced a method to determine the magnetic moment based on an inertial measurement unit combined with a non-linear least square algorithm, achieving higher accuracy in positioning the capsule [15].

Cylindrical and uniaxial PMs are commonly used because their spin does not alter the magnetic field, limiting determinable DoF to five. To overcome this limitation, various methods based on non-rotationally symmetric PMs have been proposed [16]. Song et al. suggested an improved method using two combined PMs of different sizes and opposite magnetic directions to achieve 6 DoF in PM tracking [17].

This work was supported in part by Ministry of Science and Technology, Taiwan, under Grant NSTC 112-2221-E-002-155-MY2 and in party by the National Taiwan University, under Grant NTU-CC-113L893906. The authors are with the Department of Mechanical Engineering, National Taiwan University, No. 1, Sec. 4, Roosevelt Road, Taipei, 10617, Taiwan.
*Corresponding author: chunyeonlin@ntu.edu.tw

Another approach that combines magnetic field sensing with inertial sensing [18] has been implemented in active capsule endoscopy, enabling six DoF in position estimation without necessitating complex capsule structures.

This paper presents a comprehensive study from theoretical analysis to developing a system prototype for designing a magnetic tracking system using TMR sensor arrays to estimate the orientations and locations of multiple PMs. Instead of relying on the magnetic dipole method, this paper utilizes the Gaussian-Legendre quadrature numerical integration method to calculate MFD and improve accuracy. The remainder of this article offers the following:

- A magnetic field model utilizing the Gaussian-Legendre quadrature method is introduced. An inverse model utilizing the LM optimization algorithm is employed to optimize the PMs' positions and estimate orientations.
- The development of a prototype for the PM tracking system, which incorporates TMR sensors to track two PMs, is discussed. Various parameters of the PM tracking system are compared and analyzed.

II. Permanent Magnetic Tracking System Design

Fig. 1 illustrates the proposed design of a PM tracking sensing system for estimating five DoF of location $\mathbf{T}_M$ and orientation $\mathbf{M}_P$ of the PMs. Fig. 1(a) shows the two layers of TMR sensor arrays consisting of 32 one-dimensional TMR sensors arranged orthogonally to measure the x and y-components of the MFD, B_x, and B_y, for estimating the orientation and location of the PMs. The schematic of each PM is illustrated in Fig. 1(b). The PM is a cylinder with a radius a_o and length ℓ. The centroid is at $\mathbf{T}_M$. The magnetization vector $\mathbf{M}_P$ is along the axial direction. The origin of the coordinate system is located at the centroid of the PM.

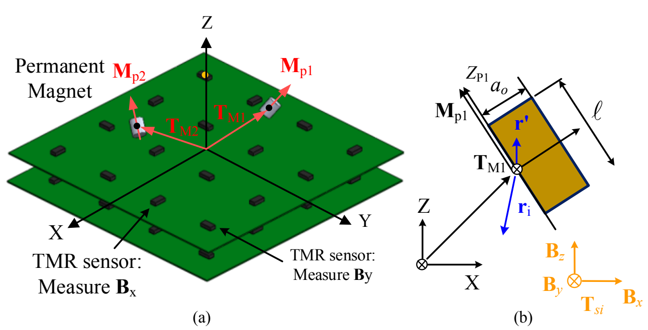

Fig. 1. Schematics of the PM tracking system. (a) TMR sensor array. (b) Variables used in our model.

A. Modeling of magnetic flux densities generated from the PMs

The magnetic flux densities (MFDs) generated from a single PM with the direction of magnetization passing through its axis can be determined by integrating the magnetic sources on the top and bottom surfaces. The magnetic flux density (MFD) generated from the PM with the direction of magnetization passing through the axis can be determined by integrating the magnetic sources on the top and bottom surfaces

$$\mathbf{B}_{PM}(\mathbf{r}) = \frac{\mu_0}{4\pi}\int_S \frac{(\hat{\mathbf{n}}\cdot\hat{\mathbf{M}})(\mathbf{r}-\mathbf{r}')}{|\mathbf{r}-\mathbf{r}'|^3}dS. \tag{1}$$

S and $\hat{\mathbf{n}}$ are the area and normal vector of the permanent magnet surfaces. $\widehat{\mathbf{M}}$ is the magnetization vector. The MFD is created at **r'** to the field point **r**. For multiple PMs, the MFDs are the sum of the MFDs generated by each PM:

$$\mathbf{B} = \sum_i \mathbf{B}_{\mathrm{PM}_i}\ . \tag{2}$$

B is the total MFD. $\mathbf{B}_{PMi}$ is the MFD generated by individual PM. In this study, the Gaussian-Legendre quadrature method is applied to calculate the surface integral of the area of a circle, where n is chosen to be three. In this paper, Gauss nodes and weights are specified as $\mathbf{x} = [-\sqrt{\frac{3}{5}}\ 0\ \sqrt{\frac{3}{5}}]^T$ and $\mathbf{w} = [\frac{5}{9}\ \frac{8}{9}\ \frac{5}{9}]^T$.

The MFD generated by the PM can be determined by using the double integration to calculate the magnetic source from the upper and lower surfaces of the PM in (3a). The numerical integration can be applied in (3b) to reduce the computational time by using the summation instead of double integration. This method can be utilized for PMs other than cylindrical ones. a_i, a_o are the inner and outer radius of the PMs. r, θ are the polar coordinate expressions of **r'**. x_d, y_d, z_d represent the x, y, z-components of **r**. x_i and x_j are the Gauss nodes used for the Gaussian Legendre quadrature method. ξ, η represent the chosen Gauss quadrature points.

$$\mathbf{B}_{\mathbf{PM}} = \frac{\mu_0}{4\pi}\iint \mathbf{g}(r,\theta)\,dr\,d\theta \tag{3a}$$

$$\mathbf{B}_{\mathbf{PM}} = \sum_{i=1}^{3}\sum_{j=1}^{3}\mathbf{g}(\xi_j,\eta_i)\boldsymbol{w}_i\boldsymbol{w}_j \tag{3b}$$

$$\text{where } \mathrm{g}(r,\theta) = \frac{r\begin{bmatrix} r\cos\theta - x_d \\ r\sin\theta - y_d \\ z - z_d\end{bmatrix}}{\left(r^2 + x_d^2 + y_d^2 + (z-z_d)^2 - 2r(x_d\cos\theta + y_d\sin\theta)\right)},$$

$$\xi_j = \left(\frac{2\pi+0}{2}\right)(1+x_j), \eta_i = \frac{a_o+a_i}{2}(1+x_i)$$

B. Inverse method of orientation and location estimation

The inverse method estimates the orientation and location of PMs using the MFDs measured by the TMR sensor array. The LM algorithm is utilized to converge the tracking orientation and location of the PMs. The number of iterations is reduced if the initial value is close to the actual pose. Therefore, the estimation from the previous state can be used as the initial value for the next state, enabling a shorter iteration process and achieving real-time tracking. However, the LM algorithm is susceptible to noise disturbances, and the iteration process increases computation time. The LM algorithm applies the Gauss-Newton method when the measurement is near the PMs and the gradient descent when the sensor is far from the PMs. A modified LM update rule using the diagonal of the Hessian matrix [19] is shown as follows:

$$\left(\mathbf{J}^T\mathbf{J}+\lambda diag\left(\mathbf{J}^T\mathbf{J}\right)\right)\boldsymbol{\delta}=\mathbf{J}^T\left[\mathbf{B}_d-f\left(\mathbf{X}\right)\right]. \quad (4)$$

f is denoted as the MFDs calculation in (1) and (2). $\mathbf{J}$ represents the Jacobian matrix of f. $\mathbf{B}_d$ is the measured MFD from the sensors. The iteration step of f can be derived through linearization. (4) is obtained by setting the derivative of the squared error between the measurements from the TMR sensors and the numerical integration forward model to zero. To determine the next step, $\boldsymbol{\delta}$ is solved by the iteration process shown in Fig. 2. In the iteration process, λ is updated by the value of ρ. By applying the trust-region algorithm, the values of ρ and v can be calculated as follows:

$$\rho=\frac{E\left(\mathbf{X}+\boldsymbol{\delta}\right)-E\left(\mathbf{X}\right)}{L\left(\boldsymbol{\delta}\right)-L\left(\mathbf{0}\right)} \quad (5a)$$

$$v=\frac{E\left(\mathbf{X}+\boldsymbol{\delta}\right)-E\left(\mathbf{X}\right)}{\boldsymbol{\delta}^T\mathbf{J}^T f(\mathbf{X})}+2 \quad (5b)$$

where $L(\boldsymbol{\delta})=E\left(\mathbf{X}\right)+\boldsymbol{\delta}^T\mathbf{J}^T f\left(\mathbf{X}\right)+\frac{1}{2}\boldsymbol{\delta}^T\mathbf{J}^T\mathbf{J}\boldsymbol{\delta}$

$L\left(0\right)=E\left(\mathbf{X}\right)$

$E(\mathbf{X})=\mathbf{B}_d-f(\mathbf{X})$

The factor ρ represents the approximation score. The iteration process of the LM algorithm and the usage of ρ and v are illustrated in Fig. 2. The upper threshold for ρ is set to 0.8, and the lower threshold is set to 0.2. E is the error function between measurement and the forward method. L(δ) represents the E after a step $\boldsymbol{\delta}$ update, while L(0) is the current value of E. The iteration process of the LM algorithm and the usage of ρ and v are illustrated in Fig. 2.

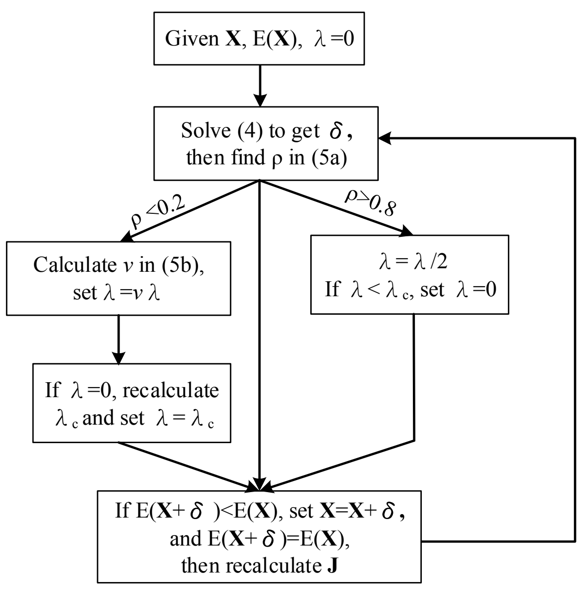

Fig. 2. Flowchart of the LM algorithm iteration process.

The process iteratively solves the problem for $\boldsymbol{\delta}$ to minimize the error between MFD measurements and the forward method. A good approximation is achieved when ρ approaches a value of one. In this case, the value of the parameter λ is reduced. Conversely, a smaller ρ leads to an increase in λ to $v\lambda$, which reduces the step size of $\boldsymbol{\delta}$ and slows down the optimization process. Using the structure of the iteration method depicted in Fig. 3, each iteration brings the estimated value closer to the actual position through a three-step process:

1) Calculate the value of the MFD $\mathbf{B}$ of the starting pose $\mathbf{t}'_s, \mathbf{m}'_s$.

2) Calculate errors by subtracting the actual value from the measurement and compare the result to the threshold $\boldsymbol{\varepsilon}$.

3) If the MFD error, calculated as the difference between the reference and the actual orientation and location, is less than ε. $\mathbf{t}'_s, \mathbf{m}'_s$ are the final solutions; otherwise, the LM algorithm is used for updating $\mathbf{t}'_s+\Delta\mathbf{t}_s$ and $\mathbf{m}'_s+\Delta\mathbf{m}_s$.

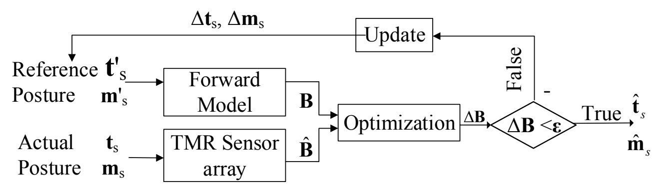

Fig. 3. Flowchart of the optimization process.

C. PM tracking system design

The PM tracking system consists of two arrays, each with 16 TMR sensors, based on the Carathéodory criterion [20]. The Cramer-Rao inequality guarantees the lower bound of the measuring variance, as indicated by Fisher Information Matrix (FIM). Consequently, the system is engineered to minimize the determinant of the FIM. The FIM is a second-order Hessian matrix expressed as follows:

$$\text{FIM}=\mathbf{J}^T\mathbf{J},$$
$$\mathbf{J}=\begin{bmatrix}\frac{\partial\mathbf{B}_1}{\partial x} & \frac{\partial\mathbf{B}_2}{\partial x} & \cdots & \frac{\partial\mathbf{B}_m}{\partial x}\\ \frac{\partial\mathbf{B}_1}{\partial y} & \ddots & & \frac{\partial\mathbf{B}_m}{\partial y}\\ \vdots & & \ddots & \vdots\\ \frac{\partial\mathbf{B}_1}{\partial\beta} & \frac{\partial\mathbf{B}_2}{\partial\beta} & \cdots & \frac{\partial\mathbf{B}_m}{\partial\beta}\end{bmatrix}, \quad (6)$$

Where m is the number of sensors; B_i represents the magnetic field measured by the TMR sensor; and $[x, y, z, \alpha, \beta]^T$ denotes the PM positions and orientation. The D-optimality criterion (7) minimizes the cost function Ψ to determine the optimal TMR sensor interval.

$$\Psi=-\log\left(\det\left(FIM\right)\right) \quad (7)$$

According to Carathéodory criterion, the choice of m sensors to estimate n parameters can be determined by

$$m=n(n+1)/2+1 \quad (8)$$

If the estimation is five-DoF, including three-DoF translations and two-DoF rotations, the sensor number is 16. The hardware configuration of the proposed PM tracking system is illustrated in Fig. 4. A TMR sensor array is tasked with estimating the MFD **B** generated by PMs. The real-time control system receives signals $\mathbf{V}_B$ from the sensors after filtering high-frequency noises using low-pass filters. The MFDs measured by the TMR sensors, $\mathbf{B}_m$, are converted into the signal $\mathbf{V}_B$, which is sent back to the personal computer (PC) to estimate the orientation and location of the PMs.

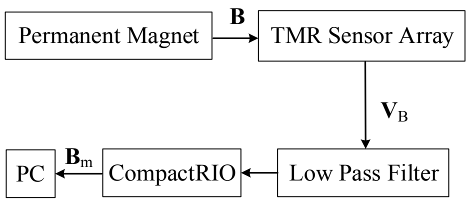

Fig. 4. Illustration of the PM tracking system.

III. NUMERICAL VERIFICATION AND VALIDATION

The PM tracking system for location and orientation estimation can be verified through numerical simulation with the following two focuses:

1) A numerical verification of the Gaussian-Legendre quadrature calculation of the MFDs generated from the PMs in different orientations and positions is performed. The parametric effects of the PMs' geometries and the layout of the TMR sensors are investigated.

2) The LM optimization algorithm is numerically validated to estimate three identical and three different-sized PMs. The optimal intervals of the magnetic sensors are discussed and analyzed.

A. Numerical verification for the Gaussian–Legendre quadrature calculation of the MFD

The Gaussian-Legendre quadrature calculation of the MFD is compared with the commercial finite element analysis software COMSOL simulation results. The simulated magnetic sensors are placed at z = -35 mm, as shown in Fig. 5(a). Figs. 5(b)-(d) show the MFDs in the x, y, and z directions, corresponding to the x and y coordinates. The model and COMSOL simulations show excellent agreement, which indicates the feasibility of using Gaussian-Legendre quadrature calculations for the PM tracking system.

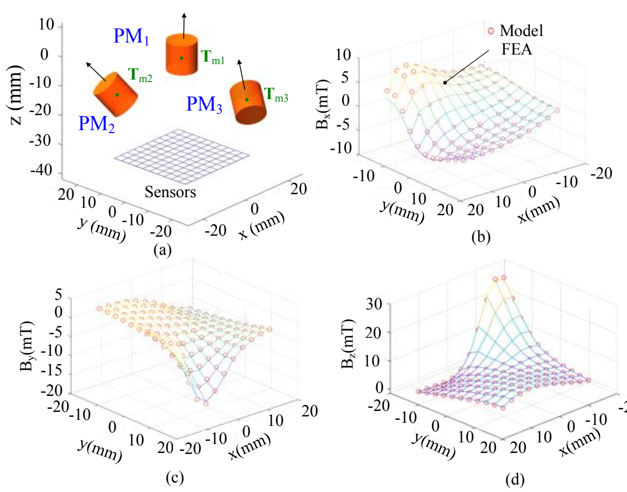

Fig. 5. Numerical investigation of multiple PMs. (a) Simulation configuration. (b) x-component. (c) y-component. (d) z-component of the MFD.

B. Numerical validation for estimation

A 4×4 magnetic sensor array is used in the simulation, as shown in Fig. 6(a). $\mathbf{T}_{mi}$ and $\mathbf{M}_{pi}$, with i=1, 2, and 3, are the location and orientation vectors of the ith PM. Three scenarios are utilized to validate the LM algorithm. Fig. 6(b) shows the simulation results of using 16 single-axis magnetic sensors to estimate the location and orientation of a single PM. For multiple PMs, 16 three-axis magnetic sensors estimate the location and orientation of three identical and different-sized PMs, as shown in Figs. 6(c) and (d). In the simulation, the MFD allowable error E(**X**) is set as 10^{-8}(T), and the state allowable error $\boldsymbol{\delta}$ is 10^{-12}.

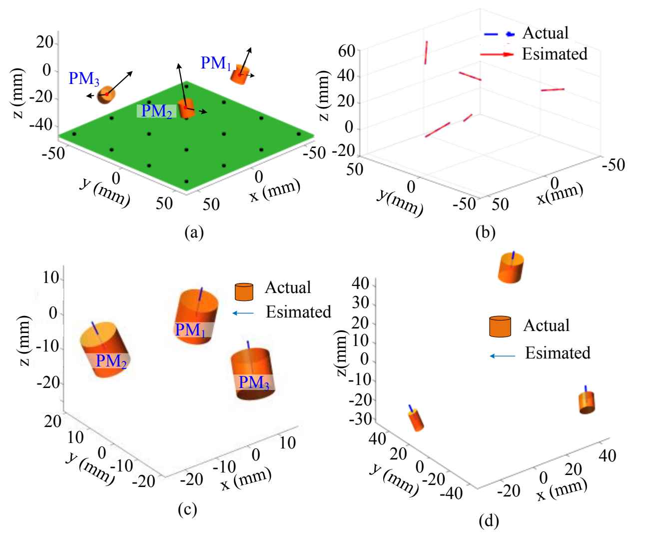

Fig. 6. Numerical validation of the estimation method. (a) Configuration. (b) A single PM. (c) Three identical PMs. (d) Three different PMs.

The configurations of the orthogonal and parallel layouts are discussed as shown in Fig. 7(a). In the orthogonal layout, the sensing directions of adjacent sensors are orthogonal, while in the parallel layout, the sensing directions are the same. Figs. 7(b) and (c) show the convergence of the residuals for these two configurations. Fig. 7(b) depicts the convergence of a single PM for three different initial values. Fig. 7(c) illustrates the convergence of two PMs in two configurations. The poses of the two PMs are [40 mm, 40 mm, 60 mm, 30˚, -60˚]^T and [-30 mm, 20 mm, 40 mm, -20˚, 30˚]^T, with initial values equal to [0 mm, 0 mm, 200 mm, 0˚, 0˚]^T. The simulation results in Figs. 7(b) and (c) reveal that both methods can converge, but the orthogonal configuration method tends to converge faster. In addition, the parallel arrangement may lead to a local minimum, causing estimation errors.

Regarding determining the distance between magnetic sensors, a wider sensor spacing increases the measurement range but decreases the resolution. The optimal distance can be calculated by finding the smallest ψ in (7). Fig. 7(d) presents a plot of ψ vs. interval for three positions: $\mathbf{X}_1$=[0 mm, 0 mm, 35 mm, 45˚, 45˚]^T, $\mathbf{X}_2$=[40 mm, 40 mm, 80 mm, 0 ˚, 0

°]^T, and $\mathbf{X}_3$=[50 mm, 50 mm, 45 mm, 50°, 15°]^T. $\mathbf{X}_1$ is positioned at the centroid point. A smaller distance between the sensors results in a smaller value of ψ. Because $\mathbf{X}_2$ and $\mathbf{X}_3$ are located at the edge, there is a curved relationship between ψ and the interval. Based on the simulation results presented in Fig. 7(d), the spacing for the developed magnetic sensor array is selected to be 35 mm, determined by the minimum value of ψ across all cases.

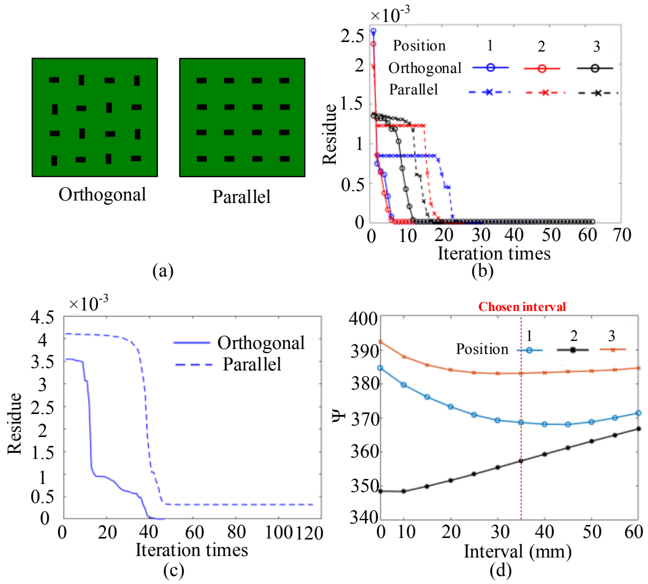

Fig. 7. Numerical investigation of the sensor layout. (a) Orthogonal and parallel configurations. (b) Different initial states. (c) Different positions. (d) Analysis of the intervals between sensors.

IV. Experimental Results and Discussion

The design of the proposed PM tracking system has been experimentally validated. Fig. 8(a) shows the experimental setup of the PM tracking system, which includes two layers of a 4×4 TMR sensor array to track the location and orientation of multiple PMs. The intervals are set at 35 mm in the horizontal direction and 11.7 mm in the vertical direction. Two different sizes of cylindrical PMs (PM_1, PM_2), with parameters detailed in Table I, are utilized to evaluate the performance of the PM tracking system.

TABLE I. Parameters for Magnetic Properties

	PM_1	PM_2	PM_3
Radius (mm)	6	4	3.25
Length (mm)	10	8	10.5
Magnetization (A/m)	807180	887520	660780

The CompactRIO-9066 real-time controller processes the TMR sensor signal captured from the voltage input module NI-9021. The sampling rate for measuring MFD is set to 100 Hz. A low-pass filter is applied to filter the magnetic signals. CompactRIO reads the MFD values from the FPGA, corrects the resulting MFD values to compensate for background MFDs, and transmits them to the PC to compute the inverse method discussed in Section II for estimating the orientation and location of the PMs. The PM tracking sensing system averages ten samples of MFDs generated from the PM, $\mathbf{B}_P$, to estimate the orientation and location of the PM. $\mathbf{B}_P$ can be obtained by subtracting the MFD generated by the background $\mathbf{B}_G$ from the measured MFD, $\mathbf{B}_M$ in (9), and $\mathbf{B}_G$ can be measured without placing PMs.

$$\mathbf{B}_P=\mathbf{B}_M-\mathbf{B}_G. \tag{9}$$

The calculations performed on a PC (Intel Core *i*7-10700F, 2.90 GHz CPU, 32 GB RAM, 64-bit OS) take about 100 ms to estimate the orientation and position. As illustrated in Fig. 8(b), the manual precision stage is capable of translational and rotational movement in all three directions (x, y, z) and two Euler angles (α, β). Fig. 8(b) shows that the PM sensing system is fixed on an acrylic frame, and the PM is placed on manual precision translation and rotation stages with 3D-printed Polylactic acid. The PM can be translated and rotated using the manual precision stages. The movement ranges in the x and y directions are 25 mm, and that in the z direction is 13 mm, with an interval of 10 µm. The ranges of rotation for the angles α and β are -15° to 15°, with a 0.1° interval. The manual precision translation stage is installed on the optical plate. The measurement range can be increased by adjusting the central fixed position of the translation stage, which leads to an experimental range of -50 to 50 mm in the x and y directions and 0-80 mm in the z direction on the optical plate. Fig. 8(c) illustrates the experimental setup using two layers of TMR sensor arrays to estimate the orientations and locations of the two PMs. Fig. 8(d) shows a PM attached to the manipulator for orientation and position estimation during its movement.

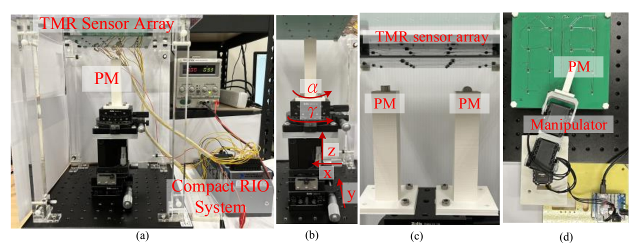

Fig. 8. PM tracking system. (a) Experimental setup. (b) Manual precision stage. (c) System side view. (d) Dynamic tracking.

Figs. 9(a) and (b) show the simulated and experimental normalized MFD of a magnetic sensor for PM_1 moving along a line and the 4×4 magnetic sensor array for a PM with the position $\mathbf{X}$=[6 mm, -10 mm, 33 mm, 0 °, 0 °]^T.

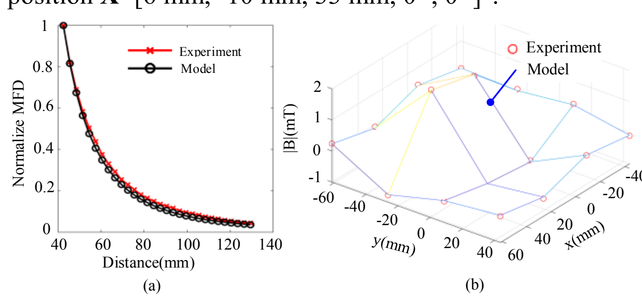

Fig. 9. Experimental results compared to MFD calculations for a single PM. (a) A moving sensor. (b) A 4×4 magnetic sensor array.

This study quantitatively evaluates the system's estimation performance based on the axial direction, aspect ratios, and repeatability. The deviation between the estimated and actual angles in the x, y, and z directions is calculated by the RMSEs. In contrast, θ_e represents the deviation between the estimated and actual angles, as defined in (10), where $\mathbf{M}_{pa}$ and $\mathbf{M}_{pe}$ are the actual and estimated PM axial directions, respectively:

$$\theta_e = \cos^{-1}\left(\frac{\mathbf{M}_{pa}^T \cdot \mathbf{M}_{pe}}{\left|\mathbf{M}_{pa}^T\right|\left|\mathbf{M}_{pe}^T\right|}\right). \tag{10}$$

Fig. 10(a) and (b) show the estimated orientations and locations of PM_1 when aligned parallel and perpendicular to the magnetic sensors, respectively. The corresponding errors in position and orientation are listed in Table II. The estimation accuracy is higher when the magnetization direction is parallel to the sensors' measurement axes due to more pronounced changes in MFDs. The RMSEs for position and orientation are maintained below 1.5 mm and 5°.

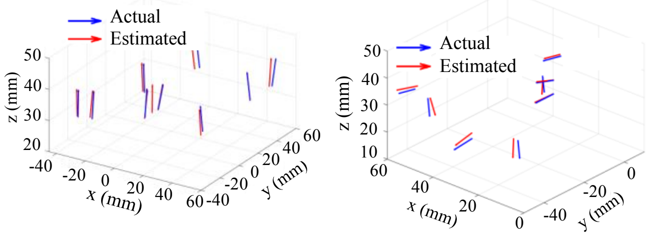

(a) (b)

Fig. 10. Experimental results in different directions: (a) parallel and (b) perpendicular.

TABLE II. ESTIMATION ERRORS FOR PARALLEL AND PERPENDICULAR DIRECTIONS

		Fig. 10(a)	Fig. 10(b)
Position (x, y, z) unit: mm	RMSE	(0.82, 0.90, 0.59)	(0.73, 0.74, 0.60)
	Max.	(1.19, 1.43, 1.25)	(1.40, 1.32, 1.20)
	Std.	(0.32, 0.43, 0.32)	(0.49, 0.43, 0.48)
Orientation unit: °	RMSE	4.7	4.86
	Max.	6.82	7.89
	Std.	1.74	2.86

Fig. 11 explores the effects of the radius-to-length ratio γ on orientation and location estimations. Figs. 11(a) and (b) show the experimental results for estimating PM_2 and PM_3, with corresponding γ values of 0.5 and 0.31, respectively. The position and orientation errors are listed in Table III. The experimental results show that the estimated position errors of PM_2 and PM_3 are close, but the orientation error of PM_3 is smaller, which suggests the orientation can be estimated with greater accuracy for the thin magnet PM_3.

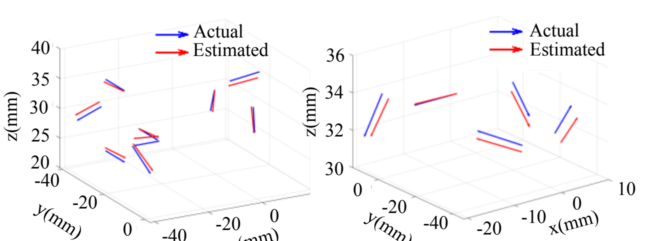

(a) (b)

Fig. 11. Experimental results for different aspect ratios: (a) thin and (b) radius-to-length ratio equal to 1.

TABLE III. ESTIMATION ERRORS FOR DIFFERENT ASPECT RATIOS

		Fig. 16(a)	Fig. 16(b)
Position (x,y,z) unit: mm	RMSE	(0.57, 0.73, 0.53)	(0.6, 0.81, 0.29)
	Max.	(1.04, 1.37, 0.77)	(0.92, 1.17, 0.51)
	Std.	(0.33, 0.46, 0.28)	(0.42, 0.54, 0.21)
Orientation unit: °	RMSE	2.96	1.86
	Max.	4	2.59
	Std.	1.05	0.83

Environmental magnetic field noise can influence estimation accuracy. A repeatability assessment was conducted involving 19 tests using the PM at five different positions and orientations, with one reference estimation for each. The RMSE, maximum, and standard deviation of errors are listed in Table IV. The estimated position errors do not surpass 0.3 mm, and orientation errors remain below 0.4°, confirming the estimation process's repeatability. Two layers of a 4×4 TMR sensor array are utilized to estimate the orientation and location of two PMs. This setup is shown in Fig. 8(c).

TABLE IV. ESTIMATION REPEATABILITY

	Position (x, y, z) unit: mm	Orientation unit: °
RMSE	(0.57, 0.73, 0.53)	(0.6, 0.81, 0.29)
Max.	(1.04, 1.37, 0.77)	(0.92, 1.17, 0.51)
Std.	(0.33, 0.46, 0.28)	(0.42, 0.54, 0.21)

Fig. 12(a) displays the experimental results for two identical PMs positioned in seven locations, with errors listed in Table V. The two-axis robotic arm shown in Fig. 8(d) facilitates the PM's motion trajectory. Fig. 12(b) details the experimental outcomes for an arc motion trajectory with a 160 mm radius and a 30° angle. The estimation operates at a 10 Hz sampling frequency, mirroring the trajectory. The position's RMSE is 1.2844 mm, with a maximum error of 1.6435 mm, while the orientation's RMSE is 4.83°, with a maximum error of 6.23°.

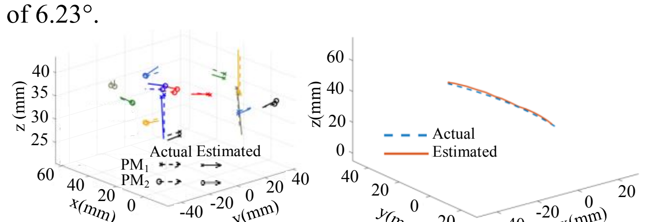

(a) (b)

Fig 12. Experimental results. (a) Estimated positions of two PMs. (b) Dynamic tracking.

TABLE V. ESTIMATION ERRORS FOR TWO PMS

		PM_1	PM_2
Position (x,y,z) unit: mm	RMSE	(0.69, 0.91, 0.64)	(1.03, 0.96, 0.51)
	Max.	(1.37, 1.50, 0.99)	(1.64, 1.52, 0.89)
	Std.	(0.43, 0.59, 0.32)	(0.56, 0.55, 0.30)
Orientation unit: °	RMSE	4.31	4.41
	Max.	6.6	8.04
	Std.	1.29	2.4

V. Conclusion

A prototype of a five-DoF tracking system for estimating locations and orientations of cylindrical PMs was developed, incorporating magnetic field modeling, the LM method, and electronic hardware design. This study utilizes the Gaussian-Legendre quadrature method for calculating magnetic fields. The LM method is applied to estimate the location and orientation for both static and dynamic object tracking. No training processes like the ANN algorithm are required. Various layouts and geometrical parameters of the PM tracking system have been explored through numerical investigations. Experiments were conducted on the prototype. The measurement rate of the developed system is 10Hz, the measurement range is 100×100×80 mm^3, and the experimental position and angle RMSEs are within 1.5 mm and 5°, respectively. The close alignment between the estimated and actual values validates the proposed PM tracking system's applicability for determining the orientation and location of two PMs. With its high-sensitivity TMR sensors, the proposed system extends the tracking range and is anticipated to meet the requirements of certain medical applications.

References

[1] H. Dai, L. Dong, B. Lv, Y. Chen, S. Song, and S. Su, "Feasibility study of permanent magnet-based tumor tracking technique for precise lung cancer radiotherapy," *IEEE Trans. Instrum. Meas.*, vol. 70, no. 4002010, pp. 1–10, Dec. 2020.

[2] S. Zeising, A. Schneider, A. Thalmayer, G. Fischer, and J. Kirchner, "A compensation method for relative movement between a sensor array and the abdomen for magnetic localization of capsule endoscopes," *IEEE Trans. Instrum. Meas.*, vol. 71, no. 4003409, pp. 1–9, 2022.

[3] V. Schlageter, P.-A. Besse, R.S. Popovic, and P. Kucera, "Tracking system with five degrees of freedom using a 2D-array of Hall sensors and a permanent magnet," *Sens. Actuator A Phys.*, vol. 92, no. 1, pp. 37–42, Aug. 2001.

[4] A. Tanwear, X. Liang, T. Böhnert, R. Ghannam, R. Ferreira, and H. Heidari, "Spintronic eyeblink gesture sensor with wearable interface system," *IEEE Trans. Biomed. Circuits Syst.*, vol. 16, no. 5, pp. 779-792, Oct. 2022.

[5] Y. Hou, L. Zheng, D. F. Wang, W. Yuan, T. Itoh, and R. Maeda, "A displacement-based TMR-type accelerometer for a high sensitivity with a wide detection range," *IEEE Sens. J.*, vol. 22, no. 20, pp. 19198-19206, Oct. 2022.

[6] K. Sun, P. Qi, X. Tao, W. Zhao, and C. Ye, "Vector magnetic field imaging with high-resolution TMR sensor arrays for metal structure inspection," *IEEE Sens. J.*, vol. 22, no. 14, pp. 14513–14521, July 2022.

[7] S. Huang, J. Luo, G. Liu, and R. Zhong, "A novel current sensing method for multicore cables using tunnel-magnetoresistance sensor array," presented at the 8th Asia Conf. on Power and Electrical Engineering (ACPEE), Tianjin, China, Apr. 2023.

[8] C. Watson and T. K. Morimoto, "Permanent magnet-based localization for growing robots in medical applications," *IEEE Robot. Autom. Lett.*, vol. 5, no. 2, pp. 2666-2673 April 2020.

[9] Z. Suna, L. Maréchal, and S. Foong, "Passive magnetic-based localization for precise untethered medical instrument tracking," *Comput Methods Programs Biomed.,* vol. 156, pp. 151–161, Mar. 2018.

[10] J. Jiang, Z. Que, K.-M. Lee, and J. Ji, "Effects of differential magnetic field/tensor and redundant measurements on multi-DOF motion estimation of a magnetic sensing system," *IEEE Sens. J.*, vol. 23, no. 15, pp. 16633–16644, Aug. 2023.

[11] S. Nedelcu and J. H. P. Watson, "Magnetic dipole model of a permanent magnet-based device," *J. Phys. D: Appl. Phys.*, vol. 34, no. 17, pp. 2622–2628, Aug. 2001.

[12] K.-M. Lee and H. Son, "Distributed multipole model for design of permanent-magnet-based actuators," *IEEE Trans. Magn.*, vol. 43, no. 10, pp. 3904–3913, Oct. 2007.

[13] S. Song, C. Hu, and M. Q.-H. Meng, "Multiple objects positioning and identification method based on magnetic localization system," *IEEE Trans. Magn.*, vol. 52, no. 10, Oct., pp. 1–4, 2016.

[14] J.W. Yi, J.J. Liu, C.L. Zhang, and X. Lu, "Magnetic motion tracking for natural human computer interaction: a review," IEEE Sensors Journal, vol. 22, no. 3 , vol. 22, no. 23, pp. 22356-22367, Dec., 2022.

[15] P. Zhang, Y. Xu, R.Z. Chen, W.G. Dong, Y. Li, R. Yu, M.Y. Dong, Z.G. Liu, Y. Zhuang, "A multimagnetometer array and inner IMU-based capsule endoscope positioning system," *IEEE Internet Things J.*, vol. 9, no. 21, pp. 21194-21203, 1 Nov.1, 2022

[16] W. Yang, C. Hu, M. Q.-H. Meng, S. Song, and H. Dai, "A six-dimensional magnetic localization algorithm for a rectangular magnet objective based on a particle swarm optimizer," *IEEE Trans. Magn.*, vol. 45, no. 8, pp. 3092–3099, Aug. 2009.

[17] S. Song, X. Qiu, and M. Q.-H. Meng, "An improved 6D pose detection method based on multiple magnets tracking," *2017 IEEE SENSORS*, Glasgow, UK, 2017, pp. 1–3.

[18] Y. Li, Z. Huang, X. Liu, Y. Jie, C. Song, and C. Hu, "Calibrated analytical model for magnetic localization of wireless capsule endoscope based on onboard sensing," *Robotica*, vol. 41, no. 5, pp. 1500–1514, Jan. 2023.

[19] A. Ranganathan. The Levenberg–Marquardt algorithm. (2004, Summer). USA: Honda Research Institute.

[20] M. Gherardini, A. Mannini, and C. Cipriani, "Optimal spatial sensor design for magnetic tracking in a myokinetic control interface," Computers in Methods and Programs in Biomedicine, vol. 211, no. 106407, pp. 1-10, Nov. 2021